Cell Reports, Volume *15*

Supplemental Information

Complexin 3 Increases the Fidelity of Signaling in a Retinal Circuit by Regulating Exocytosis at Ribbon Synapses

Lena S. Mortensen, Silvia J.H. Park, Jiang-bin Ke, Benjamin H. Cooper, Lei Zhang, Cordelia Imig, Siegrid Löwel, Kerstin Reim, Nils Brose, Jonathan B. Demb, Jeong-Seop Rhee, and Joshua H. Singer

SUPPLEMENTAL INFORMATION

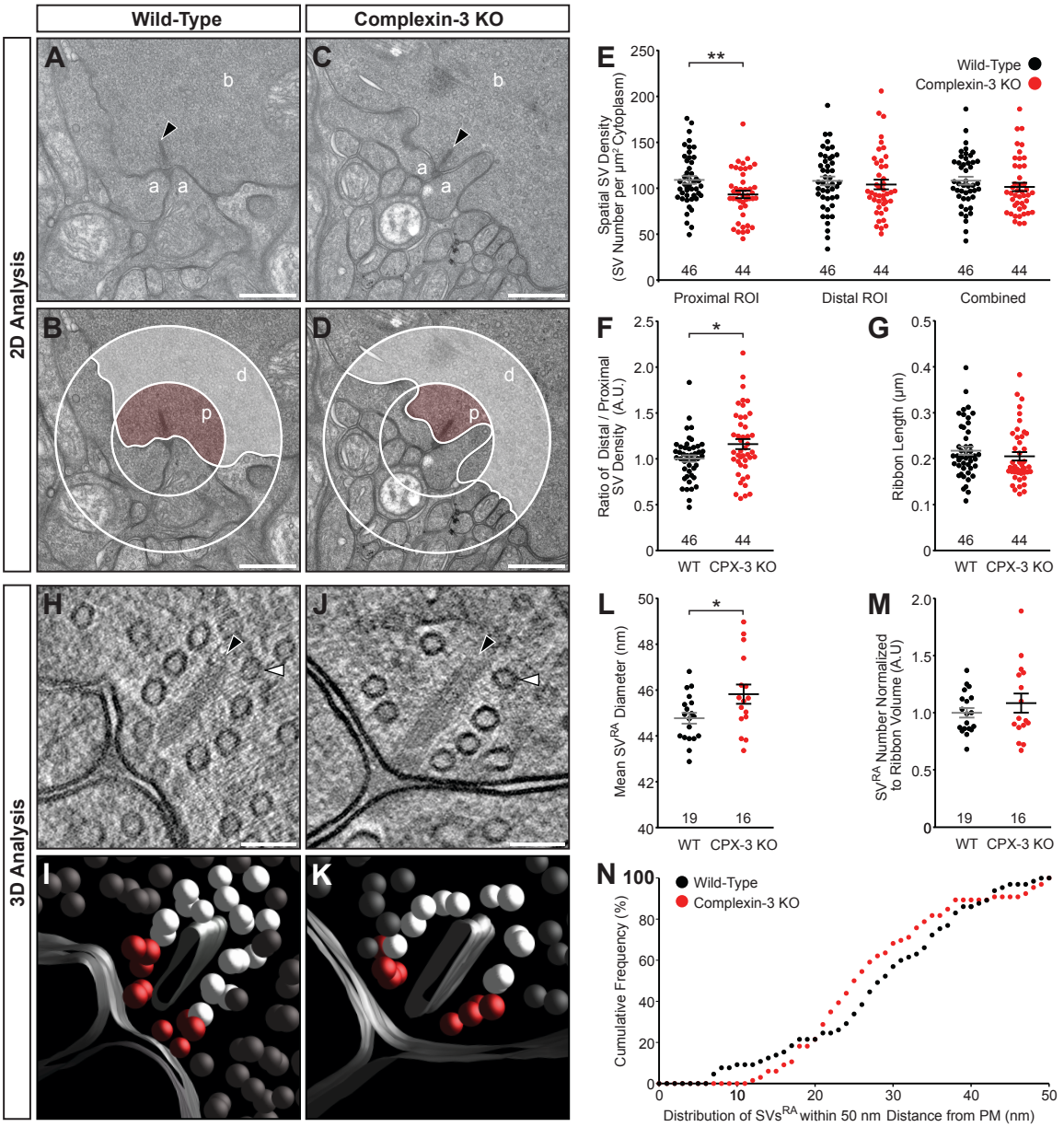

Figure S1: Ultrastructural analysis of AZ organization in RB terminals; related to Figure 1. (A and C) EM of WT and Cplx3$^{-/-}$ RB terminals. RB terminal, b; amacrine cell process, a; synaptic ribbon, arrow. (B and D) Synaptic vesicle (SV) distribution quantified as vesicle density (number/volume) in 1 and 2 µm diameter concentric arcs (proximal—p—and distal—d) centered on the ribbon base. (E) SV density in p and d regions of interest (ROIs). (F) Ratio of d to p SV densities. (G) Mean ribbon length; ribbons in both WT and Cplx3$^{-/-}$ extended same distances from plasma membrane. (H and J) Electron tomographic subvolumes of WT (n=19) and Cplx3$^{-/-}$ (n=16) synapses. Ribbon: black arrow; ribbon-associated SV: white arrow. Scale bars: A-D, 500 nm; H and J, 100 nm. (I and K) 3D models of reconstructed WT and Cplx3$^{-/-}$ ribbon profiles. Ribbon-associated SVs (SV^{RA}), white; ribbon-associated SV within 50 nm of plasma membrane, red. SV^{RA} count unchanged in Cplx3$^{-/-}$. (L) Mean diameter of SV^{RA}. (M) SV^{RA} number normalized to ribbon volume. For E-M, values mean±SEM. P values: **<0.01, *<0.05. (N) SV distribution (cumulative) within 50 nm of plasma membrane. We observed subtle differences in SV distribution: fewer within 10 nm, and more 15 to 20 nm, from plasma membrane in Cplx3$^{-/-}$ than WT. Differences, however, were not significant: maximum difference between the cumulative distributions, D, is 0.2063 with a corresponding P= 0.107 by Kolmogorov-Smirnov test.

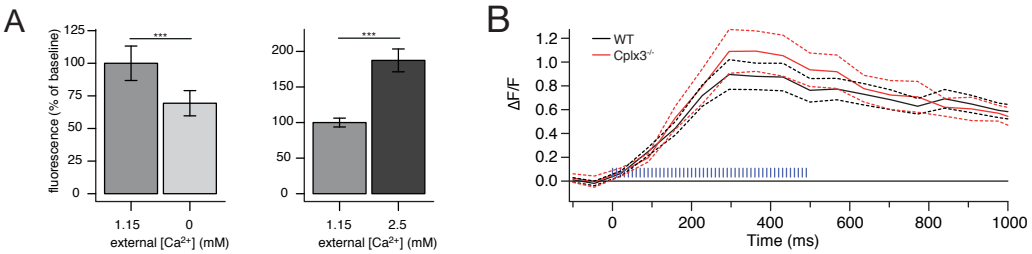

Figure S2: Imaging $[Ca^{2+}]_I$ in RB terminals; related to Figure 2. (A) Relative GCaMP3 fluorescence, a qualitative measure of $[Ca^{2+}]_I$, varies with $[Ca^{2+}]_E$ (n=30 for 1.15-->0 mM; n=10 for 1.15-->2.5 mM). *** p<0.01 by Student's t-test. (B) OGB 6F fluorescence in WT (black) and Cplx3$^{-/-}$ (red) boutons increased rapidly during stimulation, indicating a global increase in $[Ca^{2+}]_I$ following buffer saturation. Blue lines indicate train of depolarizations. The significant rise in OGB 6F fluorescence in the presence of 1 mM Bapta indicated a 10-20 fold elevation in $[Ca^{2+}]_I$ that likely arose from buffer saturation by Ca^{2+} influx; this elevation of $[Ca^{2+}]_I$ into the low micromolar range activates release modes that function independently from $[Ca^{2+}]_I$ nanodomains (Mehta et al., 2014).

SUPPLEMENTARY EXPERIMENTAL PROCEDURES

EM analysis of synapse ultrastructure

Retinae from Cplx3$^{-/-}$ and littermate Cplx3$^{+/+}$ mice (8-10 weeks old) were fixed in 4% paraformaldehyde and 2.5% glutaraldehyde (Leidig et al., 2013), embedded in 3% low-melt agarose, and vertically sectioned into 100 µm slices with a vibratome. Sections were high-pressure frozen (Leica HPM100), cryo-substituted (Leica EM AFS2) in the presence of 0.1% tannic acid and 2% osmium tetroxide, and embedded in plastic for ultramicrotomy (Imig et al., 2014).

For 2D ultrastructural analyses, electron micrographs from ultrathin plastic sections were acquired with a transmission electron microscope (Zeiss LEO 912-Omega) operating at 80 kV. For 3D tomographic analyses, 200 nm-thick sections were imaged in a JEM-2100 transmission electron microscope (JEOL) operating at 200 kV. RB terminals were identified by their size, their location in sublamina 5 of the inner plexiform layer, and their characteristic dyad synapses (Figures S1A and S1C) (Demb and Singer, 2012; Mehta et al., 2014). As noted (Reim et al., 2009), the gross morphology of the Cplx3$^{-/-}$ retina was normal.

Tomograms were reconstructed from single-axis tilt series using the IMOD package to quantify docked SVs, the morphological correlate of the RRP (Cooper et al., 2012; Imig et al., 2014; Kremer et al., 1996). Despite the resolution of EM tomography, we could not observe vesicles docked to the plasma membrane, likely owing to an artifact of the chemical fixation of specimens before high-pressure freezing; chemical fixation depletes AZ-proximate vesicles by inducing vesicle fusion and causes specimen shrinkage and membrane deformation (Korogod et al., 2015; Murk et al., 2003; Smith and Reese, 1980). High-pressure freezing of unfixed tissue, however, yielded inconsistent preservation of RB terminals, and this freezing artifact could not be eliminated. Quantifications were performed blindly using IMOD and ImageJ (Schneider et al., 2012) software. Statistical analyses were performed with GraphPad Prism (Version 6.00; GraphPad). To test for normality, the Kolmogorov-Smirnov test was used. Normally distributed data sets were compared by unpaired Student's t-tests.

Our data support observations of a normal number of ribbon-associated vesicles and a small reduction in the number of cytoplasmic vesicles in dissociated RBs treated with a Cplx3 inhibitory peptide (Vaithianathan et al., 2015). They also consistent with observations in organotypic slice cultures of synapses lacking Cplx1/2/3: these did not reveal changes in the numbers of docked and total vesicles (Imig et al., 2014). Thus, collective morphological evidence indicates that our observed deficit in phasic release was unlikely to have arisen from depletion of vesicles at AZs.

Imaging fluorescent Ca^{2+} indicators

2PLSM imaging was performed as described (Mehta et al., 2014). RBs in retinal slices were dialyzed with pipette solutions containing a Ca^{2+}-insensitive fluorescent tracer (Alexa 594 hydrazide; 0.02– 0.1 mM), the low-affinity fluorescent Ca^{2+}indicator OGB 6F (0.1 mM), and a nonfluorescent, high-affinity Ca^{2+}chelator (1 mM Bapta). Here, the effective buffering power of OGB 6F (K_D=3 μM) was insignificant given that Bapta has a 10-fold higher concentration and 50-fold higher affinity for Ca^{2+}(Naraghi and Neher, 1997).

Dyes were excited at 910 nm using a pulsed IR laser (Chameleon; Coherent), and emitted light was passed through a series of dichroic mirrors and filters and collected by GaAsP photomultipliers (Thorlabs). Collected data were analyzed using ImageJ (Schneider et al., 2012).

Changes in intracellular [Ca^{2+}] in a population of unperturbed terminals in retinal whole-mounts were assessed by imaging the genetically-encoded Ca^{2+} indicator GCaMP3 expressed in RBs (and ON CBs) by cre-mediated recombination. Tg(Pcp2-cre)1Amc/J (Barski et al., 2000; Ivanova et al., 2010) (Jackson Labs) mice were crossed with Ai38 mice in which the GCaMP3 sequence was preceded by a STOP sequence flanked by loxP sites (Madisen et al., 2012) (Jackson Labs). RB terminals were identified by their large size and position within sublamina 5 of the inner plexiform layer. 2PLSM imaging was performed as described above.

SUPPLEMENTAL REFERENCES

Barski, J.J., Dethleffsen, K., and Meyer, M. (2000). Cre recombinase expression in cerebellar Purkinje cells. Genesis *28*, 93-98.

Cooper, B., Hemmerlein, M., Ammermuller, J., Imig, C., Reim, K., Lipstein, N., Kalla, S., Kawabe, H., Brose, N., Brandstatter, J.H.*, et al.* (2012). Munc13-independent vesicle priming at mouse photoreceptor ribbon synapses. J Neurosci *32*, 8040-8052.

Demb, J.B., and Singer, J.H. (2012). Intrinsic properties and functional circuitry of the AII amacrine cell. Vis Neurosci *29*, 51-60.

Imig, C., Min, S.W., Krinner, S., Arancillo, M., Rosenmund, C., Sudhof, T.C., Rhee, J., Brose, N., and Cooper, B.H. (2014). The morphological and molecular nature of synaptic vesicle priming at presynaptic active zones. Neuron *84*, 416-431.

Ivanova, E., Hwang, G.S., and Pan, Z.H. (2010). Characterization of transgenic mouse lines expressing Cre recombinase in the retina. Neurosci *165*, 233-243.

Korogod, N., Petersen, C.C., and Knott, G.W. (2015). Ultrastructural analysis of adult mouse neocortex comparing aldehyde perfusion with cryo fixation. eLife *4*.

Kremer, J.R., Mastronarde, D.N., and McIntosh, J.R. (1996). Computer visualization of three-dimensional image data using IMOD. J Struct Biol *116*, 71-76.

Leidig, C., Bange, G., Kopp, J., Amlacher, S., Aravind, A., Wickles, S., Witte, G., Hurt, E., Beckmann, R., and Sinning, I. (2013). Structural characterization of a eukaryotic chaperone--the ribosome-associated complex. Nat Struct Mol Biol *20*, 23-28.

Madisen, L., Mao, T., Koch, H., Zhuo, J.M., Berenyi, A., Fujisawa, S., Hsu, Y.W., Garcia, A.J., 3rd, Gu, X., Zanella, S.*, et al.* (2012). A toolbox of Cre-dependent optogenetic transgenic mice for light-induced activation and silencing. Nature neuroscience *15*, 793-802.

Mehta, B., Ke, J.B., Zhang, L., Baden, A.D., Markowitz, A.L., Nayak, S., Briggman, K.L., Zenisek, D., and Singer, J.H. (2014). Global Ca^{2+} signaling drives ribbon-independent synaptic transmission at rod bipolar cell synapses. J Neurosci *34*, 6233-6244.

Murk, J.L., Posthuma, G., Koster, A.J., Geuze, H.J., Verkleij, A.J., Kleijmeer, M.J., and Humbel, B.M. (2003). Influence of aldehyde fixation on the morphology of endosomes and lysosomes: quantitative analysis and electron tomography. J Micro *212*, 81-90.

Naraghi, M., and Neher, E. (1997). Linearized buffered Ca^{2+} diffusion in microdomains and its implications for calculation of [Ca^{2+}] at the mouth of a calcium channel. J Neurosci *17*, 6961-6973.

Reim, K., Regus-Leidig, H., Ammermuller, J., El-Kordi, A., Radyushkin, K., Ehrenreich, H., Brandstatter, J.H., and Brose, N. (2009). Aberrant function and structure of retinal ribbon synapses in the absence of complexin 3 and complexin 4. J Cell Sci *122*, 1352-1361.

Schneider, C.A., Rasband, W.S., and Eliceiri, K.W. (2012). NIH Image to ImageJ: 25 years of image analysis. Nat Meth *9*, 671-675.

Smith, J.E., and Reese, T.S. (1980). Use of aldehyde fixatives to determine the rate of synaptic transmitter release. J Exp Biol *89*, 19-29.

Vaithianathan, T., Henry, D., Akmentin, W., and Matthews, G. (2015). Functional Roles of Complexin in Neurotransmitter Release at Ribbon Synapses of Mouse Retinal Bipolar Neurons. J Neurosci *35*, 4065-4070.